RESEARCH ARTICLE | DECEMBER 12 2023

Multistability and chaos in SEIRS epidemic model with a periodic time-dependent transmission rate ⊘

Special Collection: Nonlinear dynamics, synchronization and networks: Dedicated to Jürgen Kurths' 70th birthday

Eduardo L. Brugnago ✉ ⓘ ; Enrique C. Gabrick ⓘ ; Kelly C. Iarosz ⓘ ; José D. Szezech, Jr. ⓘ ;
Ricardo L. Viana ⓘ ; Antonio M. Batista ⓘ ; Iberê L. Caldas ⓘ

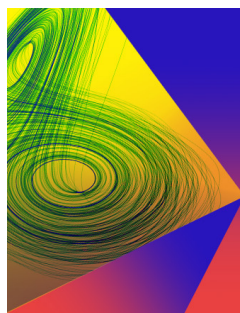🔲 Check for updates

CrossMark

🌐
View
Online

📄
Export
Citation

Multistability and chaos in SEIRS epidemic model with a periodic time-dependent transmission rate

Eduardo L. Brugnago,[1,a]   Enrique C. Gabrick,[2,b]   Kelly C. Iarosz,[1,3,4]   José D. Szezech, Jr.,[2,5]
Ricardo L. Viana,[1,6]   Antonio M. Batista,[1,2,5]   and Iberê L. Caldas[1]

AFFILIATIONS

[1] Physics Institute, University of São Paulo, 05508-090 São Paulo, SP, Brazil
[2] Graduate Program in Science, State University of Ponta Grossa, 84030-900 Ponta Grossa, PR, Brazil
[3] University Center UNIFATEB, 84266-010 Telêmaco Borba, PR, Brazil
[4] Santa Helena Institute, 84266-010 Telêmaco Borba, PR, Brazil
[5] Mathematics and Statistics Department, State University of Ponta Grossa, 84030-900 Ponta Grossa, PR, Brazil
[6] Department of Physics, Federal University of Paraná, 81531-980 Curitiba, PR, Brazil

Note: This paper is part of the Focus Issue on Nonlinear dynamics, synchronization and networks: Dedicated to Juergen Kurths' 70th birthday.
[a] **Author to whom correspondence should be addressed:** elb@if.usp.br
[b] **Electronic mail:** ecgabrick@gmail.com

ABSTRACT

In this work, we study the dynamics of a susceptible-exposed-infectious-recovered-susceptible epidemic model with a periodic time-dependent transmission rate. Emphasizing the influence of the seasonality frequency on the system dynamics, we analyze the largest Lyapunov exponent along parameter planes finding large chaotic regions. Furthermore, in some ranges, there are shrimp-like periodic structures. We highlight the system multistability, identifying the coexistence of periodic orbits for the same parameter values, with the infections maximum distinguishing by up one order of magnitude, depending only on the initial conditions. In this case, the basins of attraction have self-similarity. Parametric configurations, for which both periodic and non-periodic orbits occur, cover 13.20% of the evaluated range. We also identified the coexistence of periodic and chaotic attractors with different maxima of infectious cases, where the periodic scenario peak reaches approximately 50% higher than the chaotic one.

Published under an exclusive license by AIP Publishing. https://doi.org/10.1063/5.0156452

Seasonality is a factor that influences many infections spread. Namely, a time-dependent transmission rate leads to a non-autonomous differential equations system, enriching the dynamics and bringing features not observed in the autonomous models. Causes beyond weather seasons, such as control measures and various environmental factors, may be related to temporal variations in the transmission rate of infections. It is known that the seasonality degree is relevant to changing the epidemic system dynamics, as well as the average transmissivity. In addition, some diseases have distinct seasonality, such as annual (e.g., rubella and measles), biannual (e.g., chickenpox), and irregular (e.g., mumps) peaks. In a general picture, the seasonality frequency does not need to be linked to annual cycles. In this way, we investigate how the seasonality parameters affect the susceptible-exposed-infectious-recovered-susceptible (SEIRS) model dynamics, emphasizing the role of seasonality frequency.

I. INTRODUCTION

Mathematical models are a fundamental tool to understand the epidemic dynamics,[1] where approximations are made in order to replicate the focus behavior and provide a better understanding. Several diseases present periodic outbreaks,[2] that are related to non-constant transmission rates.[3] In this way, deterministic systems with constant transmission rate is not realistic.[4] In addition to the better description of real data, the inclusion of the non-constant term leads to chaotic solutions.[5] Non-autonomous epidemic models, with periodic transmission rates, make it possible to model the behavior of various seasonal diseases and present rich dynamics.[6–8] The chaotic solutions have a connection with reported data. For example, time series of many epidemic diseases as measles,[9] dengue,[10] mumps,[11] and others,[12] can be chaotic. Such behavior is associated with the seasonality present in recurrent infections.[13,14] In order to simulate the chaotic dynamic, a non-linear term is included in the equations,[2,15] which can be given, for example, by a square wave or

sine function.[14] The implications of chaotic regimes raise relevant questions in epidemiology,[16] where a consequence of the chaotic dynamics is a reduction of forecast horizons for new outbreaks.[1] From a mathematical modeling perspective, many of the classic epidemiological models have a compartmental structure, distributing the host population into classes according to considered stages of the disease spread evolution. Essentially, there is a compartment for the population susceptible to infection, identified by the variable S, in addition to another one for infectious individuals, identified by I. There may be several other compartments, adapting the model to the studied disease characteristics.[17,18] It is assumed these groups of individuals homogeneously distributed in the population, as well as concentrations with different contagion probabilities do not occur. Homogeneity of mean disease characteristics, such as duration of infectious and latency, is also considered. The mathematical description of a compartmental epidemiological model encompasses both: host population subdivision and transition rules between the disease stages. Secondary infections usually are described by means of an interaction term between populations in S and I compartments.

Since the seminal work of Kermack and McKendrick,[19] these models have been employed to study many diseases spread.[20–30] Formulations closer to the original proposals do not produce chaotic dynamics,[31–33] however, inclusion of multistrain[34] or seasonal[35] terms are able to reproduce chaos in a wide parameters range. Considering a susceptible-infectious-recovered (SIR) seasonal forced model, Stollenwerk *et al.*[36] investigated the dynamics of respiratory diseases, like influenza. In this case, the seasonality is related to the winter months. In their results, they found a route to chaotic dynamics via period doubling bifurcations as a function of seasonality degree, similar to the bifurcation cascade found by Yi *et al.*[35] in a SEIR forced model. However, in the second case, in addition to the chaotic dynamics, the authors obtained hyperchaotic solutions for some parameter ranges. Completely, they investigated the dynamical behavior by Poincaré sections and parameter planes assessing Lyapunov exponents. Another way to enrich the dynamics is by the time-dependent modulation of the transmission rate,[37] where the system exhibits multistability, by the coexistence of chaotic and periodic attractors for some seasonality degrees.

Bifurcation cascades as a function of various parameters in compartmental models are found in other works. Considering a SIR forced model with multistrain, Kamo and Sasaki[38] showed that the cross-immunity exerts significant influence on the dynamical behavior. For two strains, multiple attractors coexists, from which the population can switch by the introduction of small random noise in seasonal transmission. However, the complex dynamics also is present in models with one strain. In a SEIRS seasonal forced framework, Gabrick *et al.*[39] showed multistable dynamics between chaotic and periodic attractors. To evidence this, they generated hysteresis-type bifurcation diagrams as a function of the recovery and average contact rates, seasonality degree, inverse of immunity, and latent periods. Numerical simulations showed coexistence of chaotic and periodic attractors depending on the parameter range. Furthermore, by investigating the dynamical behavior as a function of the inverse of the latent period, it is possible to associate critical transitions with tipping points.[40] Once crossed this threshold, the spread diseases become chaotic.

A common characteristic of the works mentioned above is a period doubling route to chaos given as a function of the seasonality degree. However, the authors did not take into account the effects of varied seasonality frequency. Usually, seasonality is attributed to environmental factors and, as expected, it is very common to be related to the weather seasons throughout the year.[2] These seasonal forcings lead to oscillations in the infection transmission rate, being conditioned by changes in the contact rate between infectious and susceptible individuals, the circulation of infectious agents, and their infectiousness. In this study, we consider different frequencies for a seasonality function, focusing on the influence of this parameter on the system dynamics. This easing of the oscillation frequency beyond the usual seasonality, together with its amplitude, allows us to model diverse disturbances in the infection spread.

First, we obtain the disease-free (DFE) solution, which is defined by the infection eradication in the host population. The stability of this solution is associated with the *basic reproduction ratio*[17] ($\mathcal{R}_0$). Due to the non-autonomous nature of the differential equations system that describes the model, $\mathcal{R}_0$ is also time-dependent and oscillates between two extremes, bounded according to seasonality degree. In the autonomous case, for $\mathcal{R}_0 < 1$, the infection is extinguished, and otherwise, if $\mathcal{R}_0 > 1$, then the infection grows spreading in the host population. However, for non-autonomous epidemiological systems, this criterion is not directly applicable, requiring additional and more sophisticated evaluations[41] to determine the DFE solution stability. To analyze the system dynamics,[42] we compute the Lyapunov spectrum along parameter planes. Our results show a wide range of chaotic behavior in all four evaluated planes. In some regions, there are shrimp-like periodic structures[43] immersed in the chaotic bands. In addition, we find multistability. The orbit resulting from the system evolution depends on the initial conditions.[44–46] Even in periodic scenarios, the predictability of the final state is hard to be determined.[47] Also, for the same parametric configurations, we highlight the coexistence of periodic and chaotic attractors in scenarios where the maximum number of infections is higher in the periodic ones.

This article is organized as follows: In Sec. II, we explain the SEIRS model and the system formulation by its variables and parameters. After, we develop a normalized version of it and include the seasonality term, which is used throughout the study. We also present the analytical DFE solution and the time-dependent basic reproduction ratio as a function of the system parameters. In Sec. III, we present numerical results, starting with an analysis of Lyapunov exponents along parameter planes, then to attraction basins evidencing the multistability. Complementarily, we compute the proportion of initial conditions that evolve to periodic dynamics along the parameter plane formed by the average transmission rate and the seasonality frequency. Finally, Sec. IV is devoted to a brief summary of the main results and our conclusions.

II. MODEL

Typically, presented as a system of four coupled first-order ordinary differential equations, SEIRS model describes the disease spread in a host population subdivided into four compartments, which are identified as the dynamic variables S, E, I, and R, each corresponding to a portion of the population at different infection
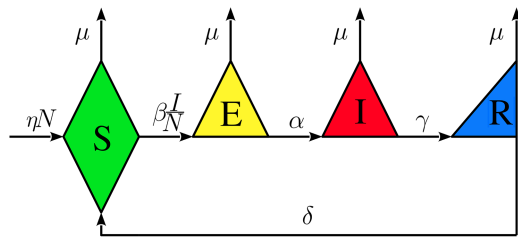
FIG. 1. Illustrative scheme of the SEIRS model. The host population is divided into compartments according to the stages of infection. System (1) dynamic variables refer to states: susceptible (S in green diamond); exposed (E in yellow triangle); infectious (I in red triangle); and recovered (R in the blue triangle). Arrows connecting compartments indicate the direction of transition between them, with the respective rates. Natural mortality (μ) just decreases the population allocated to each compartment.

stages. Given in the form[48,49]

$$\frac{dS}{dt} = \eta N + \delta R - \left(\beta \frac{I}{N} + \mu\right) S,$$

$$\frac{dE}{dt} = \beta \frac{SI}{N} - (\alpha + \mu)E,$$

$$\frac{dI}{dt} = \alpha E - (\gamma + \mu)I,$$ (1)

$$\frac{dR}{dt} = \gamma I - (\delta + \mu)R,$$

this system models the population transitions between its compartments. Note that the contagion occurs only through interaction between infectious (compartment I) and susceptible (compartment S) populations. In order to obtain epidemic scenarios, it is necessary to consider an initial condition with already exposed or infected individuals. A latency interval is considered, for which a portion of the population exposed (compartment E) to the pathogen is not yet capable to spread the infection. Once an infectious period has elapsed, individuals in I acquire temporary immunity passing to the recovered compartment (R), where they remain until become susceptible to infection again. The host population size is the sum $N = S + E + I + R$. An illustrative scheme of this transition dynamics between compartments is shown in Fig. 1.

The six parameters of the model correspond to Refs. 41, 48, and 49: host population birth rate (η); natural death rate (μ); transmission rate (β); mean latent time after the contagion ($1/\alpha$); mean infectious period ($1/\gamma$), where γ is known as recovery rate; and mean duration of immunity consequent to infection ($1/\delta$). All parameters are non-negative real numbers.

A. System normalization and inclusion of seasonality

We seek a mathematical formulation of the model that allows us to study its dynamics independently of the population size. Then, without loss of generality, we perform the following transformation of variables:[50,51]

$$S \mapsto Ns; \quad E \mapsto Ne; \quad I \mapsto Ni; \quad R \mapsto Nr,$$ (2)

where lowercase ones describe the normalized quantities and the total population $N > 0$. Adding the four equations of system (1), by means of algebraic manipulation, we obtain an expression for the exponential growth of the host population, being

$$\frac{dN}{dt} = (\eta - \mu)N.$$ (3)

From this fact and the relations proposed in (2), considering a generic variable $X = Nx$, we obtain

$$\frac{dX}{dt} = \frac{d(Nx)}{dt} = N\frac{dx}{dt} + x\frac{dN}{dt}.$$ (4)

Thus, we get the following transformation for the time derivatives:

$$\frac{dX}{dt} = N\left\{\frac{dx}{dt} + (\eta - \mu)x\right\},$$ (5)

$$\frac{dx}{dt} = \frac{1}{N}\left\{\frac{dX}{dt} - (\eta - \mu)X\right\},$$ (6)

where the uppercase X is a non-normalized system variable and the lowercase x is its normalized counterpart. Operating these transformations and, additionally, taking into account the constraint $s + e + i + r = 1$, we reduce the model to a system of three equations, given by

$$\frac{ds}{dt} = (\delta + \eta)(1 - s) - \beta si - \delta(e + i),$$

$$\frac{de}{dt} = \beta si - (\alpha + \eta)e,$$ (7)

$$\frac{di}{dt} = \alpha e - (\gamma + \eta)i,$$

whose form is identical to that arising from the constant population approximation[39] ($\eta = \mu$).

Dynamic variables normalized according to (2) represent fractions of the host population in each compartment, such that $s, e, i, r \in [0, 1]$, respecting the constraint between them. Thus, system (7) allows simulating epidemic dynamics even in non-constant population scenarios.[51]

In order to model a seasonal behavior of the transmission rate, we replace the constant parameter β by the periodic function[9]

$$\beta(t) = \beta_0 \left[1 + \beta_1 \cos(\omega t)\right],$$ (8)

such that $\beta(t)$ oscillates sinusoidally around the average transmission β_0, with a peak-to-peak variation equal to $2\beta_0\beta_1$. Throughout the text, we refer to β_1 as seasonality degree. To preserve the meaning of the epidemiological model, $\beta(t) \geq 0$ is required, hence $\beta_0 \geq 0$ and $\beta_1 \in [0, 1]$. In this study, we did not investigate the case $\beta_0 = 0$, since there is no spread of infection. Still, interested in the seasonality effects, for numerical simulations, we consider $0 < \beta_1 \leq 1$ and $\omega > 0$. We extend the idea of seasonality to periodic oscillations not necessarily corresponding to weather seasons, not even equivalent to integer multiples or submultiples of 1 year. Here, we use this term in a broader sense, referring to periodic oscillating transmission rates with any frequency.

B. Disease-free equilibrium

Disease-free equilibrium is so named to signify the disease disappearance in the host population. Assuming the fixed-point condition

$$\frac{ds}{dt}\bigg|_{P_{\text{DFE}}} = \frac{de}{dt}\bigg|_{P_{\text{DFE}}} = \frac{di}{dt}\bigg|_{P_{\text{DFE}}} = 0, \tag{9}$$

at the point $P_{\text{DFE}}(s_*, e_*, i_*)$ to system (7), we can obtain the DFE solution[17] directly solving the equations

$$0 = (\delta + \eta)(1 - s_*) - \beta s_* i_* - \delta(e_* + i_*), \tag{10}$$

$$0 = \beta s_* i_* - (\alpha + \eta)e_*, \tag{11}$$

$$0 = \alpha e_* - (\gamma + \eta)i_*. \tag{12}$$

We have that s_*, e_*, and i_* are coordinates of the fixed point, therefore, constant, and $\beta = \beta(t) = 0$ if and only if $\beta_1 = 1$ and $t = (2k+1)\pi/\omega$, with $k \in \mathbb{Z}$ and $\beta_0, \omega > 0$. Combining these facts with both Eqs. (10) and (11) implies $s_* i_* = 0$ and results $e_* = i_* = 0$ in Eqs. (11) and (12), indicating the infection extinction. As for s_*, there are two distinct cases: the first for $\delta + \eta > 0$, which gives $s_* = 1$ in Eq. (10); the second occurs if $\delta = \eta = 0$, in this case $s_* \in [0, 1]$ depends on the initial conditions. The second case is more restrictive: if $\eta = 0$, the model does not consider births and the population in non-normalized system (1) decays exponentially with the rate μ, according to Eq. (3); while $\delta = 0$ represents that infected individuals acquire permanent immunity after the infectious period, reducing the system to a SEIR model. Note that for β as a function of time, DFE is the only fixed-point solution.

The stability of this solution is related to the basic reproduction ratio $\mathcal{R}_0$.[17] For autonomous systems, this is a simple linear stability analysis based on the eigenvalues of the system's Jacobian matrix calculated in the DFE point. However, in this non-autonomous case, $\mathcal{R}_0$ is time-dependent and the eradication of infection may depend on the maximum value $\max_t\{\mathcal{R}_0(t)\}$ or, specifically, related with the basic reproduction ratio obtained for the long-term average system.[41]

C. Basic reproduction ratio

The contagion rate is associated with the prevalence or decline, and consequent future disappearance, of the infection in a host population. The system evolution to any of these scenarios is determined by the basic reproduction ratio, which, for the normalized SEIRS model according to Eq. (7), is given by

$$\mathcal{R}_0 = \alpha\beta(t) / [(\alpha + \eta)(\gamma + \eta)], \tag{13}$$

in the same way as the autonomous SEIRS,[48,49] but including an explicit time dependency in $\beta(t)$. $\mathcal{R}_0$ oscillates periodically in the range

$$\mathcal{R}_0^- \leq \mathcal{R}_0 \leq \mathcal{R}_0^+, \tag{14}$$

being the edge values defined as

$$\mathcal{R}_0^{\pm} := \frac{\alpha\beta_0(1 \pm \beta_1)}{(\alpha + \eta)(\gamma + \eta)}. \tag{15}$$

We said that $\mathcal{R}_0$ is strictly greater than unity when $\mathcal{R}_0^+ \geq \mathcal{R}_0^- > 1$ and, on the other hand, refer it to be strictly less than
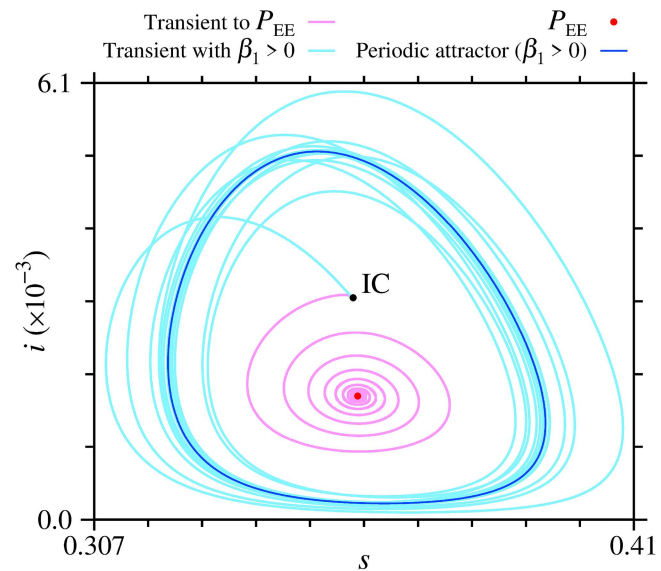
FIG. 2. Trajectories evolving from IC to the attractors in the autonomous and non-autonomous cases: pink spiral converging at P_{EE} (red dot) in the autonomous case; light blue curve converging to the periodic attractor (blue line) in the non-autonomous case. We use the fourth-order Runge–Kutta numerical integration method with a fixed step of 10^{-3}. Transients smaller than 5×10^5 integration steps being sufficient for the trajectories convergence to the attractors with great accuracy.

unity if $\mathcal{R}_0^- \leq \mathcal{R}_0^+ < 1$. For autonomous compartmental epidemiological models, it is known that $\mathcal{R}_0 < 1$ leads to the eradication of infection.[15] However, since the system is non-autonomous, specifically with the transmission rate given as a function of time, a sufficient condition for convergence to the DFE solution is the long-term basic reproduction ratio $\overline{\mathcal{R}}_0 < 1$, which is calculated over the long-term average of the system evolution.[41] Also, the point P_{DFE} is asymptotically stable if $\mathcal{R}_0^+ < 1$, i.e., verifying the parameters relation $\beta_0(1 + \beta_1) < (\alpha + \eta)(\gamma + \eta)/\alpha$.

D. Around endemic equilibrium

The autonomous SEIRS model, with $\beta \equiv \beta_0$ [equivalent to $\beta_1 = 0$ in Eq. (8)], presents a second equilibrium state, denoted by endemic equilibrium point $P_{\text{EE}}(s_e, e_e, i_e)$, in which there is no extinguishes the infection in the host population.[48] In the non-autonomous case addressed here, the trajectories can oscillate around this point. We illustrate this behavior in Fig. 2. Arises from the fixed point condition, we obtain

$$s_e = \frac{1}{\mathcal{R}_c}; \quad e_e = \frac{\gamma + \eta}{\alpha\beta_0}\varepsilon; \quad i_e = \frac{\varepsilon}{\beta_0}, \tag{16}$$

where $\mathcal{R}_c$ is the constant basic reproduction ratio, with $\beta \equiv \beta_0$ in Eq. (13), and

$$\varepsilon := \frac{(\delta + \eta)(\mathcal{R}_c - 1)}{1 + \frac{\mathcal{R}_c\delta}{\beta_0}\left[1 + \frac{\gamma + \eta}{\alpha}\right]}. \tag{17}$$

Note that, to recover a SEIR scheme from system (7), simply set $\delta = 0$, resulting in the P_{EE} for a scenario with permanent immunity.[6] Considering the autonomous model, it is necessary $\mathcal{R}_c > 0$ for P_{EE} to be attractive.[6,7] To exemplify the convergence toward endemic equilibrium, we numerically integrate the autonomous system with the following parameters: $\beta_0 = 280$, $\alpha = \gamma = 100$, $\delta = 2.5 \times 10^{-1}$, and $\eta = 2 \times 10^{-2}$. In this configuration, $\mathcal{R}_c \approx 2.799$, $s_e \approx 3.573 \times 10^{-1}$, and $i_e \approx 1.735 \times 10^{-1}$. Figure 2 shows the projection of the system's trajectories onto the $i \times s$ plane, with P_{EE} in red and a periodic orbit (blue line), which results from the evolution of the non-autonomous model with $\beta_1 = 0.1$ and $\omega = 2\pi$. Pink and light blue curves are the transient trajectories spiraling from the initial condition IC(0.3564, 0.0032, 0.0031) (highlighted point) to P_{EE} and the periodic attractor, respectively.

III. NUMERICAL RESULTS AND DISCUSSION

In this section, we numerically investigate the SEIRS model dynamics emphasizing the influence of seasonality, included according to Eq. (8). To evolve system (7), we employ the fourth-order Runge–Kutta integration method with a fixed time step of 10^{-3} and consider 5×10^5 integration steps as transient. Our simulations indicate that these settings are sufficient for the convergence of the trajectory and tangent vectors.[52,53] In particular, we check the minimum transient required in parameter planes with grids of 200×200 points, at 8 transient values from 10^3 to 5×10^6 integration steps. We found that 5×10^5 steps are enough. We also check this quantity for the other results. The time unit in the simulation is one year and the parameters have unit year^{-1}, except β_1 which is dimensionless and $[\omega] \equiv$ rad/year. We vary the parameters over wide intervals, aiming to cover characteristic values of several infections, for example, measles ($\alpha = 38.5$ and $\gamma = 100$),[54] influenza ($\alpha = 228.12$ and $\gamma = 125$),[55] and others.[56,57] We start by analyzing the Lyapunov exponents on the parameter planes shown in Subsection III A. Next, in Subsection III B, we highlight and study the system's multistability.

A. Lyapunov exponents analysis

In the present study, the system dynamics characterization is made mainly by the largest Lyapunov exponent. We verify that the SEIRS model, under the influence of a seasonal transmission rate, can evolve both to chaotic and periodic trajectories, depending on the parameters and initial conditions (see Sec. III B). To investigate the effects of seasonality frequency ω, with period $T = 2\pi/\omega$, in the system dynamics, we compute the Lyapunov spectrum along parameter planes $[\cdot] \times \omega$, where $[\cdot]$ is a model parameter. Previously, we rewrite the system (7) in autonomous form, thus, we perform the transformation $\omega t \mapsto \tau \in [0, 2\pi)$ and include the respective differential equation $d\tau/dt = \omega$. The Lyapunov spectrum is obtained by evolving the system and its respective linearized equations using the algorithm described by Wolf *et al.*[58] and the exponents sorted in descending order: $\lambda_1 \geq \lambda_2 \geq \lambda_3 \geq \lambda_4$. We adopt the initial condition $(s_0, e_0, i_0, \tau_0) = (0, 999, 0, 0, 001, 0)$ and consider 10^6 integration steps, after discarding the transient. Without prejudice, throughout the text $\tau_0 = 0$ will be omitted.

We analyze four parameter planes calculated on uniform grids of 1000×1000 points, displayed in Figs. 3 and 4. Transmissivity oscillation frequency is on the horizontal axis, which is evaluated in the range $0 < \omega \leq 6\pi$. The two largest Lyapunov exponents are represented in color: chaotic regions with $0 < \lambda_1 \leq 1.2$ (gradient from yellow to red); in periodic ones ($\lambda_1 = 0$) it shows $-1 \leq \lambda_2 < 0$, starting from white ($\lambda_2 = -1$), passing through shades of cyan to black color ($\lambda_2 = 0$).

Figure 3 illustrates two planes formed by combining ω with typical epidemiological model parameters. In Fig. 3(a), we analyze the interval $0 < \alpha \leq 400$ on the vertical axis being fixed: $\gamma = 100$, $\eta = 0.02$, $\delta = 0.25$, $\beta_0 = 270$, and $\beta_1 = 0.28$. With this parameter setting $0 < \mathcal{R}_0 \leq 3.455$, such that for $\alpha < 0.008$ the basic reproduction ratio is strictly less than unity. In the interval $0.008 < \alpha < 0.021$, we have $0.563 < \mathcal{R}_0^- < 1$ and $\mathcal{R}_0^+ > 1$. Complementarily, we obtain $1 < \mathcal{R}_0 \ \forall \ t$ with $0.021 < \alpha$ and, given the α axis discretization in steps of $\Delta\alpha = 0.4$, in Fig. 3(a), we only observe results with the basic reproduction ratio strictly greater than unity. The evolution of the system to chaotic dynamics is predominantly determined by the seasonality frequency. Seasonal cycles of less than 6 months lead predominantly to periodic behavior, see the wide dark cyan band from $\omega = 4\pi$, with small chaotic regions inserted there. For $\omega < 4\pi$ approximately vertical bands occur, revealing that latency intervals smaller than ≈ 1.3 days, corresponding to $\alpha > 280$, are of little relevance to the dynamics. Next to $\alpha = 100$ and $\omega = 2\pi$, there is a shrimp-like periodic structure, also seen around $\omega \approx \pi$. Such parameter values correspond to the latency ≈ 3.6 days and seasonality with periods $T = 1$ and $T = 2$ years, respectively. Shrimps recurrently appear in parameter planes of paradigmatic non-linear systems[59–62] from a peculiar arrangement of two saddle-node bifurcation curves and routes to chaos via period doubling.[63,64] The presence of these structures is evidence of rich dynamics and this vicinity is known to display shrimp cascades forming a repeating pattern with self-similarity.[63,65]

In Fig. 3(b), we show the plane $\gamma \times \omega$, with $50 < \gamma \leq 250$, $\alpha = 100$ and the other parameters are kept equal to those used in panel (a). For this system configuration, we calculate $\mathcal{R}_0 > 1 \ \forall \ t$ with $\gamma < 194.4$. However, in the range $194.4 < \gamma \leq 250$, we have $0.777 < \mathcal{R}_0^- < 1$ and $\mathcal{R}_0^+ > 1$. Shrimp-like periodic structures are observed in the vicinity of $\omega = \pi$ and $\omega = 2\pi$, with $\gamma \approx 100$. These periodic regions embedded in the chaotic bands are related to those in the $\alpha \times \omega$ plane. For the adopted parameters, it can be observed that the dynamics is more influenced by the infectious period than the latent one. For lower recovery rates, in the range $50 < \gamma \leq 100$ corresponding to infectious periods between ≈ 7.3 and 3.6 days, chaotic bands extend to $\omega \approx 3.5\pi$. While for periods smaller than ≈ 1.5 days, referring to $\gamma \approx 250$, the chaotic bands compress into the interval $0 < \omega \leq \pi$. Thus, for small infectious periods, chaotic trajectories occur only for seasonality with $T \geq 2$ years. Similar to what is observed in panel (a), from $\omega \approx 3.5\pi$ ($T < 6.9$ months) the analyzed parameter planes present a wide range of periodic dynamics. Cyan area taken in the intervals $50 < \gamma < 75$ and $0 < \omega \leq 6\pi$ corresponds to more stable periodic orbits, i.e. these are less sensitive to small disturbances than those obtained for higher recovery rates, notably the dark cyan region with $\gamma \to 250$.

As seen, the frequency of seasonal cycles significantly affects the SEIRS model dynamics, in addition to this factor, we highlight
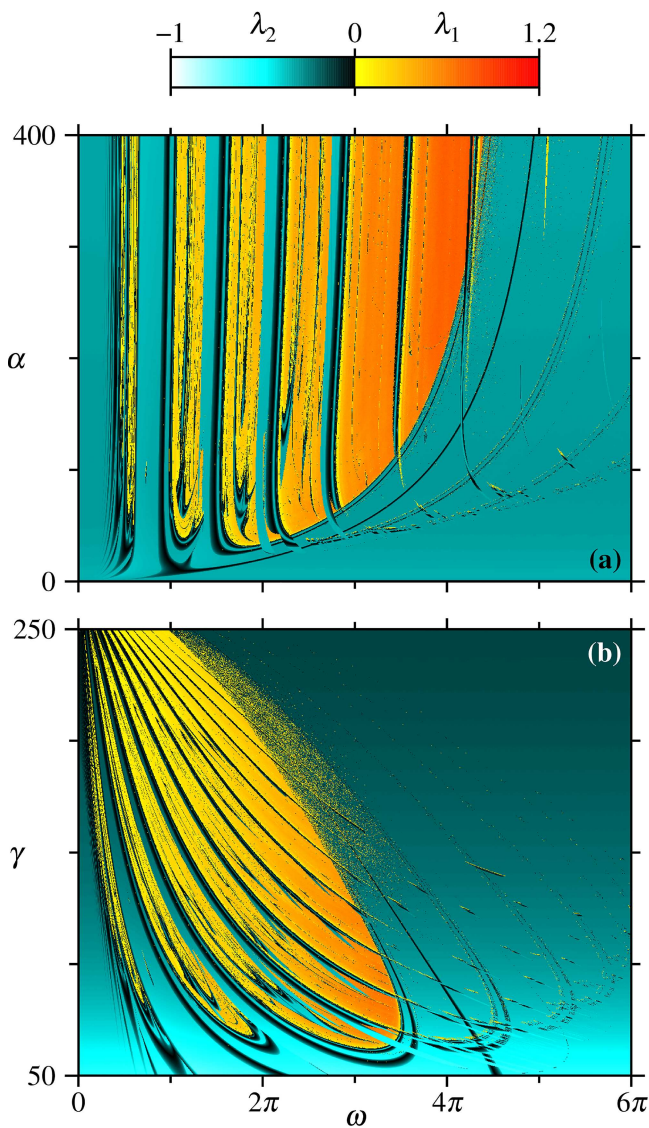
FIG. 3. Parameter planes discretized in uniform grids of 1000×1000 points. Lyapunov exponents in color, according to legend. Where $\lambda_1 = 0$, we display λ_2. Chaotic regions in the gradient from yellow to red, periodic ones in cyan shades. The horizontal axis shows the seasonality frequency. (a) The inverse of the latent period on the vertical axis. Intervals of chaotic regions in bands approximately parallel to the α axis reveal the greater relevance of ω in the system evolution. (b) Recovery rate on the vertical axis. The arrangement of the chaotic bands shows γ as a determining factor for the dynamics. Shrimp-like periodic structures close to $\alpha = \gamma = 100$ for the frequencies $\omega \approx \pi$ and $\omega \approx 2\pi$.
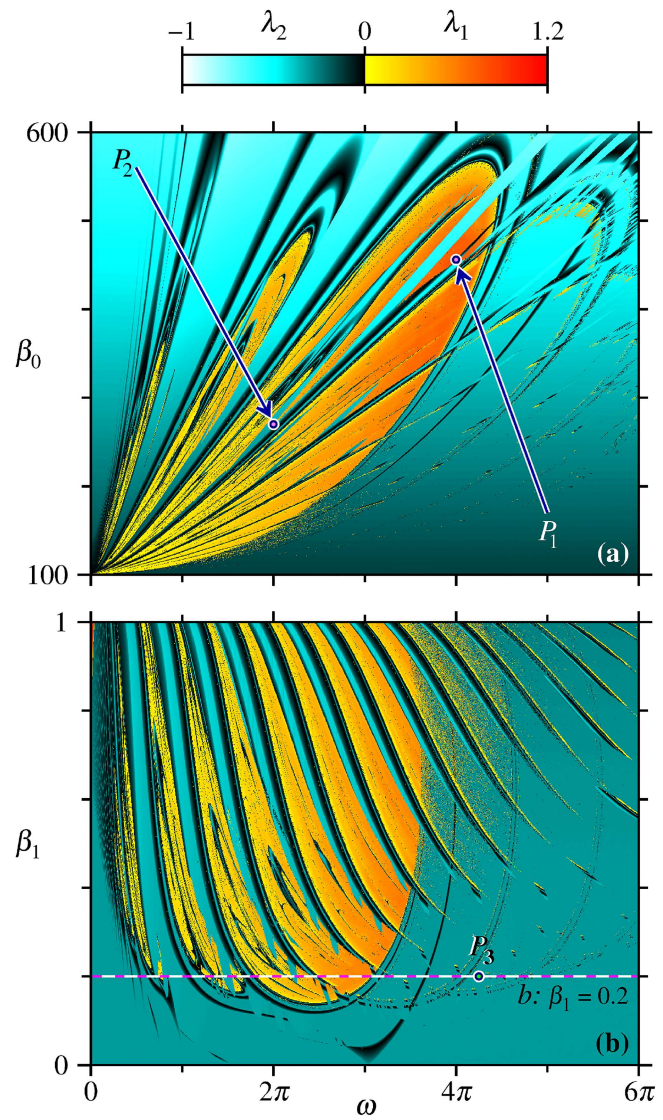

FIG. 4. Parameter planes discretized in uniform grids of 1000×1000 points. Lyapunov exponents in color, according to legend. Where $\lambda_1 = 0$, we display λ_2. Chaotic regions in the gradient from yellow to red, periodic ones in cyan shades. The horizontal axis shows the seasonality frequency. (a) Mean transmission rate on vertical axis. Diagonal periodic bands reveal the joint relevance of β_0 and ω to the system evolution. Highlighted points $P_1(4\pi, 456)$ and $P_2(2\pi, 270)$ analyzed in Subsection III B Figs. 5 and 6. (b) Seasonality degree on the vertical axis. Emphasized the segment $b: \beta_1 = 0.2$, with $0 < \omega \leq 6\pi$ (dashed line) and the point $P_3(4.25\pi, 0.2)$, for which we analyze bifurcation diagrams and attraction basins, respectively (see Fig. 8).

the effects of the mean transmission rate and the seasonality degree. Figure 4 display two planes with these parameters on the vertical axes, we set $\alpha = \gamma = 100$ and the other values equal to those used in Fig. 3, being in panel (a) $\beta_1 = 0.28$ and in (b) $\beta_0 = 270$. Figure 4(a) comprises the interval $100 < \beta_0 \leq 600$ on the vertical axis, in it we

see a periodic region around $\omega = 2\pi$ and $\beta_0 = 300$ immersed in a chaotic band. This shrimp-like structure corresponds to that shown in Fig. 3(b). Mean transmission rate increasing ($\beta_0 \to 600$) is associated with the occurrence of very stable periodic orbits ($\lambda_2 < -0.5$). On the other hand, also for large transmissivities, with $300 < \beta_0$

13 December 2023 00:23:34

< 550 and around $\omega = 4\pi$, the chaotic trajectories occur with the highest values of λ_1 (colors from orange to red). In the $\beta_0 \times \omega$ plane evaluated section, the periodic bands are interspersed diagonally with the chaotic ones, such that the system evolution depends both on the mean transmission rate and on its frequency. In this range of β_0, the basic reproduction ratio varies between $\mathcal{R}_0^- \approx 0.720$ and $\mathcal{R}_0^+ \approx 7.677$. For values of $\beta_0 > 138.944$ results $\mathcal{R}_0 > 1 \ \forall \ t$. In the interval $100 < \beta_0 < 138.944$, we get $0.720 < \mathcal{R}_0^- < 1$ and $\mathcal{R}_0^+ > 1$. Points $P_1(4\pi, 456)$ and $P_2(2\pi, 270)$, highlighted in Fig. 4(a), are targets of the multistability analysis shown in Subsection III B.

Figure 4(b) illustrates the influence of β_1 in the SEIRS model dynamics. We consider the interval $0 < \beta_1 \leq 1$ on the vertical axis, where the transmission rate oscillates from the minimum $\beta_0(1 - \beta_1)$ to the maximum $\beta_0(1 + \beta_1)$ within one period T. Here, $0 < \mathcal{R}_0 < 5.398$, where $\mathcal{R}_0$ is strictly greater than unity for $0 < \beta_1 < 0.629$. In the seasonality degree range $0.629 < \beta_1 \leq 1$, the edge values are $0 \leq \mathcal{R}_0^- < 1$ and $\mathcal{R}_0^+ > 1$. We observe a pattern of chaotic bands interspersed with periodic ones, similar to that displayed in Fig. 3(a). However, β_1 is more relevant to the dynamics than the parameter α, increasing its influence to higher frequencies of seasonal cycles from $\omega \approx \pi$. In Subsection III B, we evidence the system multistability along the segment highlighted in $\beta_1 = 0.2$ (magenta and white dashed line) and for the point $P_3(4.25\pi, 0.2)$.

B. Multistability and coexistence of chaotic and periodic attractors

System (7) with periodic $\beta \equiv \beta(t)$ presents multistability,[39] i.e., different orbits can occur for a given parametric configuration, depending on the initial condition.[45] Given this feature, in addition to the unpredictability due to chaotic trajectories, the coexistence of chaotic and periodic attractors is observed, as well as distinct periodic orbits. Additionally to the varied dynamic behaviors, slightly different starting conditions can lead to more pronounced peaks in the infectious curve. In this subsection, we investigate multistability in the model, especially for the parameter values highlighted in Subsection III A. All basins of attraction shown below employ a uniform grid plane discretization of 1000×1000 points.

Figure 5 exhibits two attractors projected in the plane $i \times s$, one chaotic (magenta line) and other periodic (blue line), both at the point $P_1(\omega, \beta_0) = P_1(4\pi, 456)$ shown in Fig. 4(a). The chaotic attractor is generated from the initial condition $C_1 = (0.990, 0.001, 0.009)$ and shows the maximum infectious population proportion $i_{max} \approx 0.02$. For the periodic one, we adopt the initial condition $C_2 = (0.998, 0.001, 0.001)$, resulting in the maximum value $i_{max} \approx 0.032$. The periodic case recurrently leads to peaks of infections $\approx 50\%$ greater than the maximum observed in the chaotic situation. If, on the one hand, predictability facilitates the planning of epidemic containment protocols, on the other hand, a greater number of cases can cause harm to public health. However, both chaotic and periodic orbits present the same time average of cases $\langle i \rangle_t \approx 2.1 \times 10^{-3}$.

For the point $P_2(\omega, \beta_0) = P_2(2\pi, 270)$, also displayed in Fig. 4(a), we perform a scan of initial conditions and distinguish the obtained orbits between chaotic and periodic ones. To that end, we uniformly vary the initial values of infectious (i_0) and exposed (e_0). Figure 6 illustrates the plane $e_0 \times i_0$ with $0 < e_0, i_0 \leq 1$ and
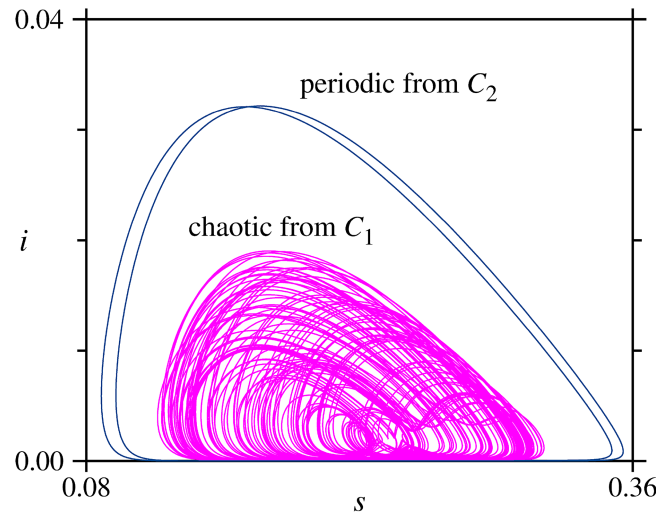

FIG. 5. Plane $i \times s$ projection of attractors obtained for the point $P_1(4\pi, 456)$, highlighted in Fig. 4(a). Chaotic attractor (magenta line) obtained from the initial condition $C_1 = (0, 990, 0, 001, 0, 009)$ and periodic one (blue line) resulting from the initial condition $C_2 = (0.998, 0.001, 0.001)$. For the chaotic case, the maximum value of infectious agents is $i_{max} \approx 0.02$, in the periodic one it is $i_{max} \approx 0.032$.

$s_0 = 1 - (e_0 + i_0)$. Basins are identified in colors, where pairs (i_0, e_0) that lead to chaotic attractors are in black and those that lead to periodic behavior are in blue. The gray region is outside the model domain. We find $\approx 53.5\%$ of valid initial conditions (outside the gray region) leading to chaotic behavior. Pairs (e_0, i_0) that evolve to periodic attractors have a sum $0.471 \leq e_0 + i_0 \leq 0.824$ and, consequently, $0.176 \leq s_0 \leq 0.529$. These proportions of infectious and exposed individuals are very high for the initial phase of an epidemic, even so, when it comes to dynamic analysis, these data help to understand the basins of each behavior and are especially valuable for the development of epidemic control protocols.

Similar to what is verified for the point P_1, for P_2, we find a periodic orbit with a higher peak of infectious agents than the chaotic one, as shown in Fig. 7. The chaotic attractor (magenta) is obtained from the same initial condition C_2 adopted in Fig. 5, the periodic one (blue) results from the condition $C_3 = (0.399, 0.001, 0.6)$. The maximum infectious case in the chaotic scenario is $i_{max} \approx 0.037$, although in the periodic trajectory, we have $i_{max} \approx 0.048$. Both scenarios present approximately the same time average of cases, being $\langle i \rangle_t \approx 1.7 \times 10^{-3}$.

Figure 8(a) concatenates 100 bifurcation diagrams along segment $b : \beta_1 = 0.2$, in the frequency interval $0 < \omega \leq 6\pi$ uniformly discretized in 1000 points, see dashed line in Fig. 4(b). For each value of ω, 100 trajectories are generated from randomly assigned initial conditions in the interval $0 < e_0, i_0 < 1$, drawn in a uniform distribution and respecting the restriction $e_0 + i_0 \leq 1$, being $s_0 = 1 - (e_0 + i_0)$. Once the transient has been discarded, we continue to evolve the system for 10^6 integration steps and select the local maxima i_p (peak value) in the infectious time series over the last 7.5×10^4 steps, equivalent to the last 75 years in simulation. In
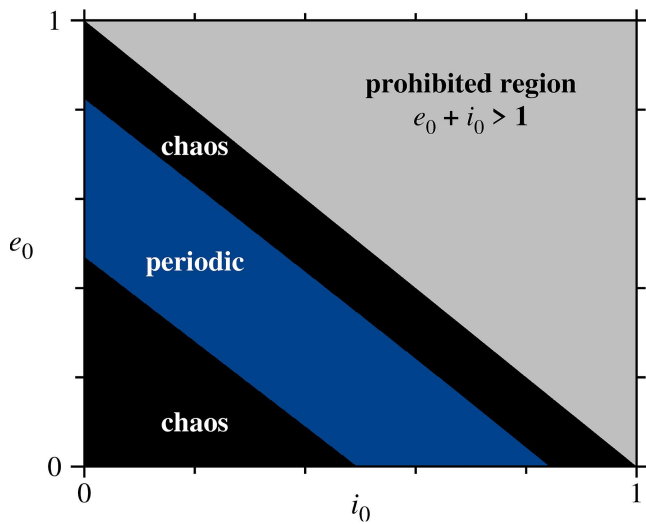
FIG. 6. Plane $e_0 \times i_0$ of initial conditions discretized in uniform grid of 1000×1000 points. Parametric configuration of point $P_2(2\pi, 270)$. In gray, we identify the region outside the model domain. Of all evaluated valid initial conditions, $\approx 46.5\%$ evolve to be periodic orbits (blue bands) and the remaining $\approx 53.5\%$ leads to chaotic ones (black color).
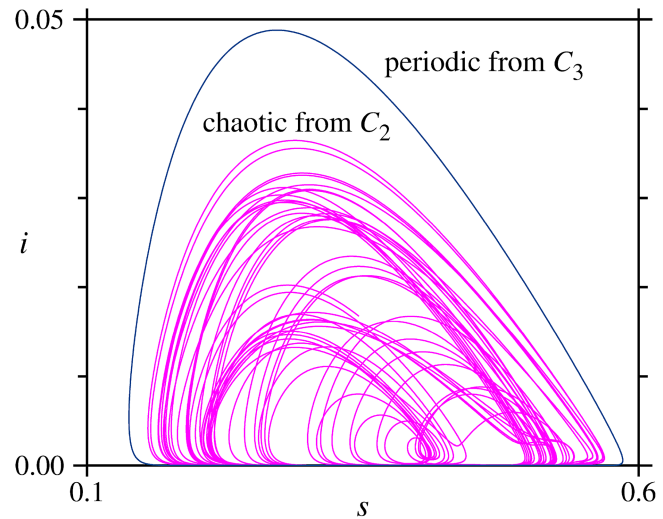

FIG. 7. Plane $i \times s$ projection of attractors obtained for the point P_2. Chaotic attractor (magenta line) results from the initial condition $C_2 = (0.998, 0.001, 0.001)$, periodic one (blue line) arising from $C_3 = (0.399, 0.001, 0.6)$. The chaotic presents a maximum of infectious $i_{max} \approx 0.037$ and the periodic one has $i_{max} \approx 0.048$.

this way, we construct a set $\mathcal{I}_k(\omega)$ of the local maxima in $i(t)$ curves, for given ω and the k-th initial condition. If there are periodic attractors, it can occur $\mathcal{I}_j(\omega) = \mathcal{I}_{k \neq j}(\omega)$, reducing the total amount of sets. Given the k-th initial condition C_k, we have

$$i_p(\omega; C_k) := i(t_p, \omega; C_k), \qquad (18)$$

being

$$\left.\frac{di}{dt}\right|_{t_p} = 0 \text{ and } \left.\frac{d^2i}{dt^2}\right|_{t_p} < 0. \qquad (19)$$

Then, we define these sets as

$$\mathcal{I}_k(\omega) := \left\{ i_p(\omega; C_k) : t_p \in \mathcal{T} \right\}, \qquad (20)$$

where $\mathcal{T}$ is the evaluation time interval. Complementarily, we identify each different set through its maximum value

$$i_{max}(\omega; C_k) := \max\{\mathcal{I}_k(\omega)\}. \qquad (21)$$

In Fig. 8(a), we plot all the distinct $\mathcal{I}_k(\omega)$ sets. By means of i_{max} it is possible to distinguish different orbits that occur for the same parametric configuration, where we use the color code for such identification. This distinction is effective between periodic orbits and is also useful for highlighting points corresponding to smaller chaotic attractors from larger ones. Figure 8(a) displays the coexistence of distinct chaotic orbits in the band starting at $\omega \approx 2.5\pi$ and goes to $\omega \approx 3\pi$, where chaotic attractors occur with $i_{max} \approx 0.030$ (orange dots) and others with $i_{max} \approx 0.020$ (cyan and teal dots), depending on the initial conditions. For higher frequencies, we observe a vast coexistence interval of periodic attractors, for example, in $\omega = 4.25\pi$ (vertical dashed line), there are 3 periodic orbits: period 1, with $i_{max} \approx 0.003$ (black color); period 3, with $i_{max} \approx 0.012$

(teal color); and period 2, with $i_{max} \approx 0.030$ (orange color). High peaks of infectious are obtained for $\omega \approx 1.5\pi$ and $\omega \approx 0.7\pi$, where $i_p \approx 0.04$, i.e., the local maxima in the infectious time series reach, periodically, nearly 4% of the host population.

The coexistence of orbits with such a discrepancy in the maximum value of infectious, as seen in Fig. 8(a), evidencing the initial condition's influence not only on the system dynamic regime but also determining the system evolution to scenarios with a greater or lesser number of infected individuals, arriving at the difference in the order of magnitude. Figure 8(b) displays the attraction basins of the three listed periodic attractors for $\omega = 4.25\pi$, corresponding to the point $P_3(\omega, \beta_1) = P_3(4.25\pi, 0.2)$, shown in Fig. 4(b). Initial conditions on plane $e_0 \times i_0$ are in the same intervals and grid configuration as in Fig. 6. The color code used to identify the 3 different basins is similar to the one employed in the bifurcation diagram, there is a slight difference in color tone to facilitate visualization. Pairs (i_0, e_0) that lead to period 1 orbit (with $i_{max} \approx 0.003$) are in black color; those leading to the period 3 orbit (with $i_{max} \approx 0.012$) are in teal color; and those that evolve to period 2 orbit (with $i_{max} \approx 0.030$) are in orange color. The gray region contains the pairs outside the normalized system domain (prohibited region). Notable are the alternating diagonal bands of the attraction basins. The highlight region in the bottom left corner, bounded by the white and magenta dashed box, is amplified in Fig. 9(a) followed by two magnifications, in which the self-similarity and intricate nature of the attraction basins obtained for P_3 is evident.

The succession of magnifications shown in Fig. 9 starts in the region marked in Fig. 8(b) and proceeds to scan intervals of initial conditions one order of magnitude smaller per panel, with the area covered in each successor being 10^{-2} times that of the previous one. Color code is the same as Fig. 8(b), identifying the i_{max} of
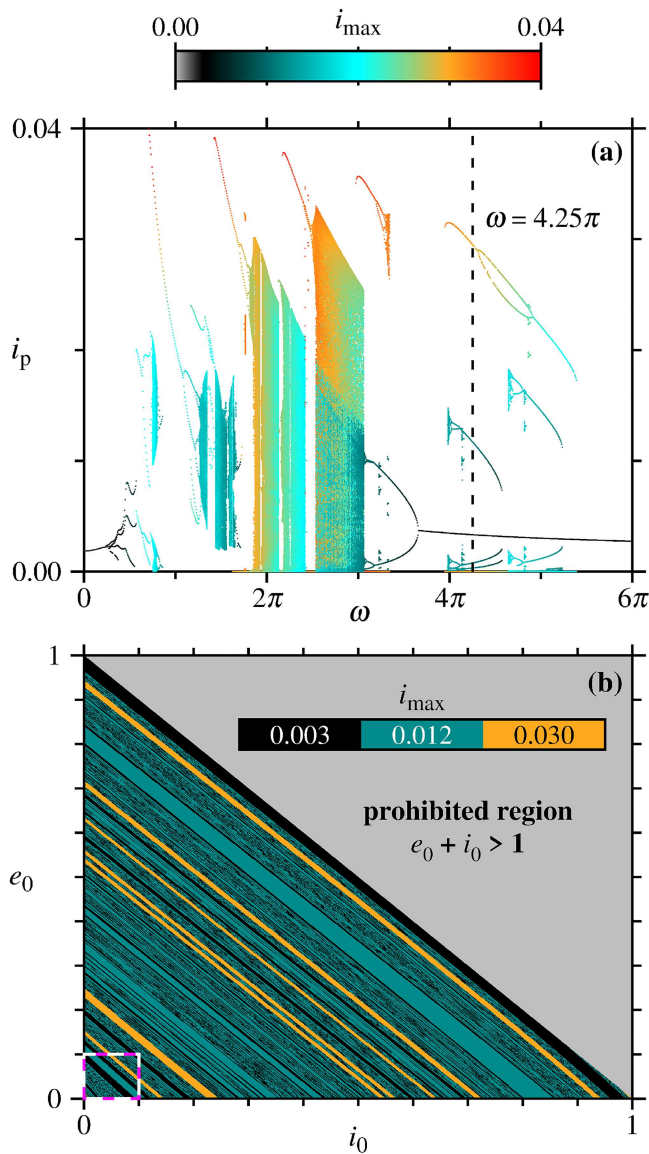
FIG. 8. (a) Concatenated bifurcation diagrams of 100 initial conditions for each ω value along segment b_1, dashed line in Fig. 4(b). The horizontal axis is discretized into 1000 equidistant points. Plotted all distinct $\mathcal{I}_k(\omega)$. Color code for $i_{max}(\omega; C_k)$ distinguishing attractors, according Eq. (21). For $\omega = 4.25\pi$ (dashed line) there are 3 periodic attractors, this point corresponds to $P_3(4.25\pi, 0.2)$ in Fig. 4(b). (b) Basins of attraction in the initial conditions plane $e_0 \times i_0$ discretized in the uniform grid of 1000×1000 points, with $s_0 = 1 - (e_0 + i_0)$ and parametric configuration for P_3. The gray region is outside of the normalized system domain. Dashed square in the bottom left corner is magnified in Fig. 9(a).

FIG. 9. Attraction basins in a succession of magnifications. Axes discretized in uniform grid of 1000×1000 points. Color code identifies the maximum infectious value i_{max} of each attractor, as defined in Eq. (21). (a) Magnification of the delimited region in Fig. 8(b), with $0 < e_0, i_0 \leq 10^{-1}$. Box in bottom left corner enlarged on panel (b) $0 < e_0, i_0 \leq 10^{-2}$. In turn, the highlighted box is magnified in (c) $0 < e_0, i_0 \leq 10^{-3}$.

the attractor resulting from each pair (e_0, i_0). Table I presents the area percentage occupied by each basin of attraction for all three evaluated ranges of initial conditions.

First, in Fig. 9(a), we evaluate the initial conditions interval $0 < e_0, i_0 \leq 10^{-1}$, where 46.75% of the points lead to smallest
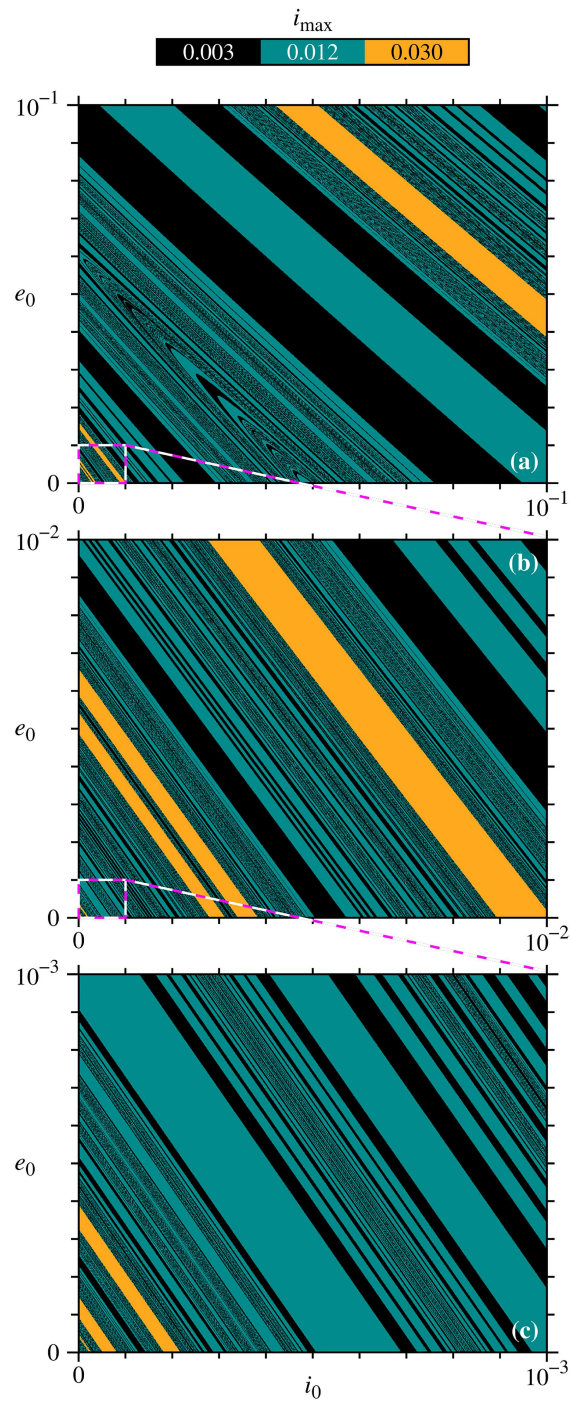
TABLE I. Area percentage occupied by each basin of attraction for the three evaluated regions. First column identifies the panel in Fig. 9, and the second column informs the respective range of initial conditions.

Panel	$e_0, i_0 \in$	i_{max}		
		0.003	0.012	0.030
a	$(0, 10^{-1}]$	46.75%	47.78%	5.47%
b	$(0, 10^{-2}]$	40,32%	44,02%	15,66%
c	$(0, 10^{-3}]$	32,39%	65,97%	1,64%

i_{max} orbit and 5.47% of them belong to the attraction basin of the periodic attractor with highest infectious peak. The box at the bottom left corner is enlarged in panel (b), where $0 < e_0, i_0 \leq 0,10^{-2}$. In this region, the basin of attraction corresponding to $i_{max} \approx 0.003$ occupying 40,32% of the total area, and the highest infectious peak attractor results from 15,66% of the initial conditions. Panel (c) shows the last magnification, performed in the interval $0 < e_0, i_0 \leq 0,10^{-3}$, being 65.97% of the area occupied by the basin of period 3 attractor, with the maximum of infectious ≈ 0.012. In this sample, only 1.64% of the total area leads to $i_{max} \approx 0.030$. Given the discretization and intervals of both axes in Fig. 9(c), one-point variation, being the increment of 10^{-6} either vertically or horizontally, represents a difference of 1 individual in 1 million of the host population for the initial condition of infectious or exposed. Resulting in significantly different maximum infectious values for this small change, with greater sensitivity for e_0 and i_0 of smaller orders of magnitude.

Finally, in Fig. 10, we obtain a fraction of initial conditions that result in periodic orbits for points along the parameter plane $\beta_0 \times \omega$. We use the same intervals and parametric configuration of Fig. 4(a). For each pair (ω, β_0), we draw 100 equiprobable initial conditions in the interval $0 < e_0, i_0 < 1$, respecting the constraint $e_0 + i_0 \leq 1$. Similar to what is made to obtain the bifurcation diagram in Fig. 8(a), starting from the k-th initial condition C_k, we evolve the system by 10^6 integration steps even after the transient and evaluate only the last 7.5×10^4 trajectory points. In this section of the time series, we select the local maxima in the $s(t)$, $e(t)$ and $i(t)$ curves and check the periodicity with an accuracy of 10^{-6}. Period 12 is considered the maximum. We do not focus on determining the period of each orbit, but just identify if it is periodic or not and, subsequently, compute the fraction $\rho_{per}(\omega, \beta_0)$ of initial conditions that lead to periodic behavior.

In the sense explained above, Fig. 10 consolidates information from 100 parameter planes, each associated with the k-th initial condition for every pair (ω, β_0). We represent ρ_{per} by the color code. Pairs in this plane for which all evaluated initial conditions result in periodic orbits ($\rho_{per} = 1$) are in black color. The ones that 100% led to non-periodic attractors ($\rho_{per} = 0$) are in red color. Intermediate cases are on the gradient from red to yellow ($\rho_{per} = 0.25$) and white ($\rho_{per} = 0.5$) and, on the other side, from white to cyan ($\rho_{per} = 0.75$) and black. In the small gray region (bottom left corner), the sample of time series is not enough to determine periodicity, or deny it, due to the high period of oscillations. Regions with some fraction of non-periodic behavior, where $\rho_{per} < 1$, resemble the bands of

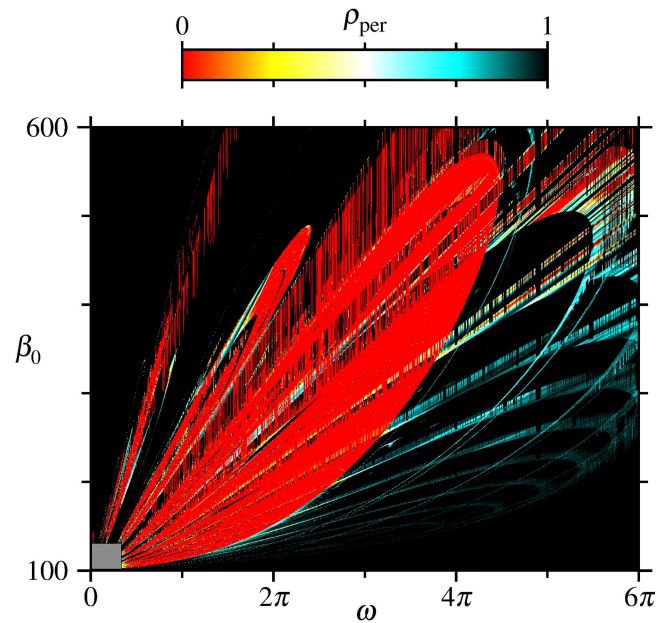**FIG. 10.** In colors, the fraction $\rho_{per}(\omega, \beta_0)$ of the trajectories that evolve to periodic dynamics, from 100 randomly assigned initial conditions. Parameter plane discretized in uniform grid of 1000×1000 points, with $0 < \omega \leq 6\pi$ and $100 < \beta_0 \leq 600$. The coexistence of periodic and non-periodic orbits ($0 < \rho < 1$) is observed in 13.20% of the valid area. In the gray square region, the time series sampling was not enough to verify periodicity.

$\lambda_1 > 0$ shown in Fig. 4(a). Unlike the initial condition considered in Subsection III A, here the exposed initial value is not null. Furthermore, accuracy, sampling, and the maximum period adopted result in some differences between this and that parameter plane.

The cyan bands in Fig. 10, as well as the small yellow regions, demonstrate the coexistence of periodic and non-periodic orbits, related to seasonality parameters. Through this assessment, we obtain only periodic orbits for 61.50% of the valid area (subtracting the gray region), exclusively non-periodic along 25.30%, and both behaviors coexist in 13.20% of the parameter plane.

IV. CONCLUSION

We numerically investigated the SEIRS model dynamics under a time-dependent transmission rate. Such temporal dependence is periodic and consists of expanding the concept of seasonality, considering different periods in addition to those that synchronize with the climatic seasons. Through parameter planes combining the seasonality frequency and typical epidemiological model parameters, we evidenced the chaotic dynamics occurrence, referring to various analyses of reported data suggesting that some epidemics have chaotic behavior.[9,11,66] Focusing on the transmission rate function, we highlight the coexistence of chaotic and periodic orbits for certain parametric configurations, as well as a diversity of periodic attractors. We found that chaotic orbits may present lower infectious peaks than periodic ones, even so with the same temporal average of

infectious cases. Assuming it is a disease that affects humans (which is not a premiss of the model), the predictability of periodic orbits facilitates the planning of public health campaigns. On the other hand, the lowest maximum number of cases in the chaotic attractor may represent a benefit when it comes to reduce the infection spread. In terms of modeling real-world infections based on the system studied in this work, it is necessary to consider the precision, which the parameters can be determined, since in the parameter planes there are narrow periodic bands immersed in chaotic regions. Also, in the vicinity of the shrimp-like structures, cascades of similar periodic regions occur, entering in scales of very small parametric variations, in such a way that small changes in the parameters can lead to a drastic change in the dynamic behavior.

The system presents a multistability of periodic orbits with different periods showing marked differences in the maximum infected values. By means of attraction basins, obtained for certain parametric configurations, we showed that small variations of the initial conditions can lead to different orders of magnitude of the maximum infectious agents number. Furthermore, for a wide range of frequency and average transmissivity settings, orbits of periods up to 12 coexist with larger periods and even non-periodic ones. Those two features of the system, present chaotic dynamics and multistability, lead to challenges for proposals of epidemic control since chaotic dynamics reduce predictability and the multistable character can lead to significantly different periodic orbits through small changes of the initial conditions. The oscillation frequency of the transmission rate proved to be relevant to the system dynamics, being one of the determining factors for the occurrence of chaos. Seasonality parameters also influence oscillations in the infectious curve in periodic scenarios, resulting in different counts of local maxima within a period. An investigation of this relationship can be carried out using isospike diagrams, however, is far from the focus of the present study, so we consider it for future work.

ACKNOWLEDGMENTS

AUTHOR DECLARATIONS

Conflict of Interest

The authors have no conflicts to disclose.

Author Contributions

Eduardo L. Brugnago: Conceptualization (equal); Data curation (equal); Formal analysis (equal); Investigation (equal); Methodology (equal); Software (equal); Writing – original draft (equal); Writing – review & editing (equal). **Enrique C. Gabrick:** Conceptualization (equal); Formal analysis (equal); Investigation (equal); Methodology (equal); Writing – original draft (equal); Writing – review & editing (equal). **Kelly C. Iarosz:** Conceptualization (equal); Writing – review & editing (equal). **José D. Szezech Jr.:** Writing – review & editing (equal). **Ricardo L. Viana:** Conceptualization (equal); Formal analysis (equal); Supervision (equal); Writing – review & editing (equal). **Antonio M. Batista:** Conceptualization (equal); Formal analysis (equal); Supervision (equal); Writing – review & editing (equal). **Iberê L. Caldas:** Formal analysis (equal); Supervision (equal); Writing – review & editing (equal).

DATA AVAILABILITY

The data that support the findings of this study are available from the corresponding author upon reasonable request.

REFERENCES

[1] M. J. Keeling and P. Rohani, *Modeling Infectious Diseases in Humans and Animals*, 1st ed. (Princeton University Press, Princeton, NJ, 2008).
[2] S. Altizer, A. Dobson, P. Hosseini, P. Hudson, M. Pascual, and P. Rohani, "Seasonality and the dynamics of infectious diseases," Ecol. Lett. **9**, 467–484 (2006).
[3] N. C. Grassly and C. Fraser, "Seasonal infectious disease epidemiology," Proc. R. Soc. B **273**, 2541–2550 (2006).
[4] D. Greenhalgh and I. A. Moneim, "SIRS epidemic model and simulations using different types of seasonal contact rate," Syst. Anal. Model. Simul. **43**, 573–600 (2003).
[5] B. T. Grenfell, B. M. Bolker, and A. Kleczkowski, "Seasonality and extinction in chaotic metapopulations," Proc. R. Soc. B **259**, 97–103 (1995).
[6] J. L. Aron and I. B. Schwartz, "Seasonality and period-doubling bifurcations in an epidemic model," J. Theor. Biol. **110**, 665–679 (1984).
[7] I. B. Schwartz and H. L. Smith, "Infinite subharmonic bifurcation in an SEIR epidemic model," J. Math. Biol. **18**, 233–253 (1983).
[8] Y. A. Kuznetsov and C. Piccardi, "Bifurcation analysis of periodic SEIR and SIR epidemic models," J. Math. Biol. **32**, 109–121 (1994).
[9] L. F. Olsen and W. M. Schaffer, "Chaos versus noisy periodicity: Alternative hypotheses for childhood epidemics," Science **249**, 499–504 (1990).
[10] M. Aguiar, S. Ballesteros, B. W. Kooi, and N. Stollenwerk, "The role of seasonality and import in a minimalistic multi-strain dengue model capturing differences between primary and secondary infections: Complex dynamics and its implications for data analysis," J. Theor. Biol. **289**, 181–196 (2011).
[11] W. P. London and J. A. Yorke, "Recurrent outbreaks of measles, chickenpox and mumps: I. Seasonal variation in contact rates," Am. J. Epidemiol. **98**, 453–468 (1973).
[12] M. J. Keeling, P. Rohani, and B. T. Grenfell, "Seasonally forced disease dynamics explored as switching between attractors," Phys. D **148**, 317–335 (2001).
[13] M. Aguiar, N. Stollenwerk, and B. W. Kooi, "Torus bifurcations, isolas and chaotic attractors in a simple dengue fever model with ADE and temporary cross immunity," Int. J. Comput. Math. **86**, 1867–1877 (2009).
[14] G. Tanaka and K. Aihara, "Effects of seasonal variation patterns on recurrent outbreaks in epidemic models," J. Theor. Biol. **317**, 87–95 (2013).
[15] O. N. Bjørnstad, *Epidemics: Models and Data Using R*, 1st ed. (Springer, Cham, 2018), pp. XIII, 312.
[16] D. A. Rand and H. B. Wilson, "Chaotic stochasticity: A ubiquitous source of unpredictability in epidemics," Proc. R. Soc. B **246**, 179–184 (1991).
[17] R. M. Anderson and R. M. May, *Infectious Diseases of Humans: Dynamics and Control* (Oxford University Press, 1991).
[18] E. C. Gabrick, P. R. Protachevicz, A. M. Batista, K. C. Iarosz, S. L. T. de Souza, A. C. L. Almeida, J. D. Szezech, Jr., M. Mugnaine, and I. L. Caldas, "Effect of two vaccine doses in the SEIR epidemic model using a stochastic cellular automaton," Phys. A **597**, 127258 (2022).
[19] W. O. Kermack and A. G. McKendrick, "A contribution to the mathematical theory of epidemics," Proc. R. Soc. London, Ser. A **115**, 700–721 (1927).

[20]D. J. D. Earn, P. Rohani, B. M. Bolker, and B. T. Grenfell, "A simple model for complex dynamical transitions in epidemics," Science **287**, 667–670 (2000).

[21]M. Aguiar, B. Kooi, and N. Stollenwerk, "Epidemiology of dengue fever: A model with temporary cross-immunity and possible secondary infection shows bifurcations and chaotic behaviour in wide parameter regions," Math. Model. Nat. Phenom. **3**, 48–70 (2008).

[22]S. H. Ho, D. He, and R. Eftimie, "Mathematical models of transmission dynamics and vaccine strategies in Hong Kong during the 2017–2018 winter influenza season," J. Theor. Biol. **476**, 74–94 (2019).

[23]M. Amaku, D. T. Covas, F. A. B. Coutinho, R. S. A. Neto, C. Struchiner, A. Wilder-Smith, and E. Massad, "Modelling the test, trace and quarantine strategy to control the COVID-19 epidemic in the state of São Paulo, Brazil," Infect. Dis. Model. **6**, 46–55 (2021).

[24]C. Manchein, E. L. Brugnago, R. M. da Silva, C. F. O. Mendes, and M. W. Beims, "Strong correlations between power-law growth of COVID-19 in four continents and the inefficiency of soft quarantine strategies," Chaos **30**, 041102 (2020).

[25]E. L. Brugnago, R. M. da Silva, C. Manchein, and M. W. Beim, "How relevant is the decision of containment measures against COVID-19 applied ahead of time?," Chaos, Solitons Fractals **140**, 110164 (2020).

[26]R. Amelia, N. Anggriani, A. K. Supriatna, and N. Istifadah, "Mathematical model for analyzing the dynamics of tungro virus disease in rice: A systematic literature review," Mathematics **10**, 2944 (2022).

[27]N. Dalal, D. Greenhalgh, and X. Mao, "A stochastic model for internal HIV dynamics," J. Math. Anal. Appl. **341**, 1084–1101 (2008).

[28]J. Dushoff, J. B. Plotkin, S. A. Levin, and D. J. D. Earn, "Dynamical resonance can account for seasonality of influenza epidemics," Proc. Natl. Acad. Sci. U.S.A. **101**, 16915–16916 (2004).

[29]J. A. Galvis, C. A. Corzo, J. M. Prada, and G. Machado, "Modeling between-farm transmission dynamics of porcine epidemic diarrhea virus: Characterizing the dominant transmission routes," Prev. Vet. Med. **208**, 105759 (2022).

[30]M. Mugnaine, E. C. Gabrick, P. R. Protachevicz, K. C. Iarosz, S. L. de Souza, A. C. Almeida, A. M. Batista, I. L. Caldas, J. D. Szezech, Jr., and R. L. Viana, "Control attenuation and temporary immunity in a cellular automata SEIR epidemic model," Chaos, Solitons Fractals **155**, 111784 (2022).

[31]I. Cooper, A. Mondal, and C. G. Antonopoulos, "A SIR model assumption for the spread of COVID-19 in different communities," Chaos, Solitons Fractals **139**, 110057 (2020).

[32]S. L. de Souza, A. M. Batista, I. L. Caldas, K. C. Iarosz, and J. D. Szezech, Jr., "Dynamics of epidemics: Impact of easing restrictions and control of infection spread," Chaos, Solitons Fractals **142**, 110431 (2021).

[33]A. M. Batista, S. L. T. de Souza, K. C. Iarosz, A. C. L. Almeida, J. D. Szezech, Jr., E. C. Gabrick, M. Mugnaine, G. L. dos Santos, and I. L. Caldas, "Simulation of deterministic compartmental models for infectious diseases dynamics," Rev. Bras. Ensino Fis. **43**, e20210171 (2021).

[34]S. Bianco, L. B. Shaw, and I. B. Schwartz, "Epidemics with multistrain interactions: The interplay between cross immunity and antibody-dependent enhancement," Chaos **19**, 043123 (2009).

[35]N. Yi, Q. Zhang, K. M. D. Yang, and Q. Li, "Analysis and control of an SEIR epidemic system with nonlinear transmission rate," Math. Comput. Modell. **50**, 1498–1513 (2009).

[36]N. Stollenwerk, S. Spaziani, J. Mar, I. E. Arrizabalaga, D. Knopoff, N. Cusimano, V. Anam, A. Shrivastava, and M. Aguiar, "Seasonally forced SIR systems applied to respiratory infectious diseases, bifurcations, and chaos," Comput. Math. Methods **2022**, 3556043 (2022).

[37]S. Bilal, B. K. Singh, A. Prasad, and E. Michael, "Effects of quasiperiodic forcing in epidemic models," Chaos **26**, 093115 (2016).

[38]M. Kamo and A. Sasaki, "The effect of cross-immunity and seasonal forcing in a multi-strain epidemic model," Phys. D **165**, 228–241 (2002).

[39]E. C. Gabrick, E. Sayari, P. R. Protachevicz, J. D. Szezech, Jr., K. C. Iarosz, S. L. T. de Souza, A. C. L. Almeida, R. L. Viana, I. L. Caldas, and A. M. Batista, "Unpredictability in seasonal infectious diseases spread," Chaos, Solitons Fractals **166**, 113001 (2023).

[40]E. S. Medeiros, I. L. Caldas, M. S. Baptista, and U. Feudel, "Trapping phenomenon attenuates the consequences of tipping points for limit cycles," Sci. Rep. **7**, 42351 (2017).

[41]J. Ma and Z. Ma, "Epidemic threshold conditions for seasonally forced SEIR models," Math. Biosci. Eng. **3**, 161 (2006).

[42]T. Tél and M. Gruiz, *Chaotic Dynamics: An Introduction Based on Classical Mechanics*, 1st ed. (Cambridge University Press, Cambridge, 2006).

[43]V. dos Santos, J. D. Szezech, Jr., M. S. Baptista, A. M. Batista, and I. L. Caldas, "Unstable dimension variability structure in the parameter space of coupled Hénon maps," Appl. Math. Comput. **286**, 23–28 (2016).

[44]U. Feudel, C. Grebogi, B. R. Hunt, and J. A. Yorke, "Map with more than 100 coexisting low-period periodic attractors," Phys. Rev. E **54**, 71–81 (1996).

[45]U. Feudel and C. Grebogi, "Multistability and the control of complexity," Chaos **7**, 597–604 (1997).

[46]U. Feudel, "Complex dynamics in multistable systems," Int. J. Bifurcation Chaos **18**, 1607–1626 (2008).

[47]C. Grebogi, S. W. McDonald, E. Ott, and J. A. Yorke, "Final state sensitivy: An obstruction to predictability," Phys. Lett. A **99**, 415–418 (1983).

[48]K. Rock, S. Brand, J. Moir, and M. J. Keeling, "Dynamics of infectious diseases," Rep. Prog. Phys. **77**, 026602 (2014).

[49]O. N. Bjørnstad, K. Shea, M. Krzywinski, and N. Altman, "The SEIRS model for infectious disease dynamics," Nat. Methods **17**, 557–558 (2020).

[50]D. Greenhalgh, "Hopf bifurcation in epidemic models with a latent period and nonpermanent immunity," Math. Comput. Modell. **25**, 85–107 (1997).

[51]M. Y. Li, J. R. Graef, L. Wang, and J. Karsai, "Global dynamics of a SEIR model with varying total population size," Math. Biosci. **160**, 191–213 (1999).

[52]G. Benettin, L. Galgani, A. Giorgilli, and J.-M. Strelcyn, "Lyapunov characteristic exponents for smooth dynamical systems and for Hamiltonian systems; a method for computing all of them. Part 1: Theory," Meccanica **15**, 9–20 (1980).

[53]I. Shimada and T. Nagashima, "A numerical approach to ergodic problem of dissipative dynamical systems," Prog. Theor. Phys. **61**, 1605–1616 (1979).

[54]Z. Bai and Y. Zhou, "Global dynamics of an SEIRS epidemic model with periodic vaccination and seasonal contact rate," Nonlinear Anal. Real World Appl. **13**, 1060–1068 (2012).

[55]A. Cori, A. J. Valleron, F. Carrat, G. Scalia Tomba, G. Thomas, and P. Y. Boëlle, "Estimating influenza latency and infectious period durations using viral excretion data," Epidemics **4**, 132–138 (2012).

[56]J. Lessler, N. G. Reich, R. Brookmeyer, T. M. Perl, K. E. Nelson, and D. A. T. Cummings, "Incubation periods of acute respiratory viral infections: A systematic review," Lancet Infect. Dis. **9**, 291–300 (2009).

[57]P. E. Sartwell, "The distribution of incubation periods of infectious disease," Am. J. Epidemiol. **51**, 310–318 (1950).

[58]A. Wolf, J. B. Swift, H. L. Swinney, and J. A. Vastano, "Determining Lyapunov exponents from a time series," Phys. D **16**, 285–317 (1985).

[59]J. A. C. Gallas, "Structure of the parameter space of the Hénon map," Phys. Rev. Lett. **70**, 2714 (1993).

[60]V. Castro, M. Monti, W. B. Pardo, J. A. Walkenstein, and E. Rosa, Jr., "Characterization of the Rössler system in parameter space," Int. J. Bifurcation Chaos **17**, 965–973 (2007).

[61]R. Barrio, F. Blesa, S. Serrano, and A. Shilnikov, "Global organization of spiral structures in biparameter space of dissipative systems with Shilnikov saddle-foci," Phys. Rev. E **84**, 035201 (2011).

[62]P. C. Rech, "How to embed shrimps in parameter planes of the Lorenz system," Phys. Scr. **92**, 045201 (2017).

[63]J. A. C. Gallas, "Dissecting shrimps: Results for some one-dimensional physical models," Phys. A **202**, 196–223 (1994).

[64]R. Varga, K. Klapcsik, and F. Heged us, "Route to shrimps: Dissipation driven formation of shrimp-shaped domains," Chaos, Solitons Fractals **130**, 109424 (2020).

[65]J. A. C. Gallas, "Structure of the parameter space of a ring cavity," Appl. Phys. B **60**, 279 (1995).

[66]A. Jones and N. Strigul, "Is spread of COVID-19 a chaotic epidemic?," Chaos, Solitons Fractals **142**, 110376 (2021).